AIAA JOURNAL
Vol. 47, No. 9, September 2009

Active Aeroelastic Control Over a Multisurface Wing: Modeling and Wind-Tunnel Testing

A. De Gaspari,* S. Ricci,† L. Riccobene,‡ and A. Scotti§
Politecnico di Milano, 20156 Milano, Italy

DOI: 10.2514/1.34649

This paper presents the work that has been performed on a wind-tunnel aeroelastic wing model to implement a multisurface modal control system. Wing model realization, the control system, and experimental setup were described briefly here, together with a methodology used to numerically tune the simple control system. Usage of a multiple wind-tunnel test session has been adopted first to perform numerical–experimental correlations and then to optimize control parameters. The entire control system demonstrates the capability to damp the wing bending and torsion modes while still remaining stable within the flight envelope.

Nomenclature

$\ddot{b}_i$	=	bending acceleration of wing strip i
C	=	command torque
C_s	=	generalized damping matrix
c	=	reference chord
$\mathbf{f}$	=	generalized unsteady aerodynamic force term
G	=	actuator driver gain
GR_{ijk}	=	gear ratio related to control surface i, mode j, and wing strip k
G_{ij}	=	gain related to mode i and wing strip j
$H_{ag}(k, M_\infty)$	=	unsteady aerodynamic gust frequency response matrix
$H_{am}(k, M_\infty)$	=	unsteady aerodynamic frequency response matrix
H_δ	=	servoactuator transfer functions
i	=	winding current
J	=	rotor inertia
K_e, K_t	=	voltage constant and torque constant
K_P, K_I, K_D, K_{D2}	=	proportional integral derivative (PID) controller gains
K_s	=	generalized stiffness matrix
k	=	reduced frequency $=\omega \cdot c/2V_\infty$
L	=	inductance
l_i	=	distance from accelerometer on control surface i to wing elastic axis
M_s	=	generalized mass matrix
M_∞	=	Mach number
q	=	dynamic pressure
$\mathbf{q}$	=	generalized coordinate
R, L	=	winding resistance and inductance
$\mathbf{r}$	=	virtual states vector
T_f	=	friction torque
V	=	command voltage
V_g	=	gust vertical velocity
V_∞	=	flight speed
v	=	input voltage
$\mathbf{x}_a$	=	aerodynamic states
$\mathbf{x}_{ae}$	=	aeroelastic states
$\ddot{Z}_i$	=	acceleration measurement on control surface i
$\delta_{c,i}$	=	imposed rotation on control surface i
δ_i	=	rotation of control surface i
$\ddot{\theta}_i$	=	torsion acceleration of wing strip i
ξ	=	poles damping
ξ_f	=	pseudointegrator damping
τ	=	gear-head gear ratio
ω	=	shaft angular velocity
ω_f	=	pseudointegrator natural frequency

Presented as Paper 2138 at the 48th AIAA/ASME/ASCE/AHS/ASC Structures, Structural Dynamics, and Materials Conference, Honolulu, Hawaii, 23–26 April 2007; received 18 September 2007; revision received 5 June 2009; accepted for publication 5 June 2009.

*Ph.D. Candidate, Department of Aerospace Engineering, Via La Masa 34; degaspari@aero.polimi.it.

†Associate Professor, Department of Aerospace Engineering, Via La Masa 34; sergio.ricci@polimi.it.

‡Ph.D. Candidate, Department of Aerospace Engineering, Via La Masa 34; riccobene@aero.polimi.it.

§Research Assistant, Dipartimento di Ingegneria Aerospaziale, Via La Masa 34. Member AIAA.

I. Introduction

THE usage of multiple control surfaces on airplane wings has different aims: to perform static aeroelastic control and/or dynamic control. When dealing with static aeroelasticity, the first kind of action turns out to be devoted to improving the structural deformation of a wing, by means of load distribution control. Controlling lift distribution along a span, as already documented [1–3], can allow induced drag reduction during cruise flight and better load distribution along the entire wing box, thus making the entire system more efficient. Dynamic control over the wing is devoted to suppressing any possible initial flutter occurrence, to permit, at first, efficient maneuvers for the aircraft (for example, minimizing stresses on critical structural points, such as wing–fuselage connections) and to damp structural vibrations. Actuation and control of multiple surfaces along the wing span and on a complete airplane thus becomes one way of realizing more advanced aircraft, taking into account the ever increasing levels of energy-cost reduction related to flight activity and, of course, flight safety and comfort. The main examples of this approach are probably represented by NASA Active Flexible Wing (A.F.W.) and Active Aeroelastic Wing (A.A.W.) programs [4,5], where differential deflection of multiple wing control surfaces placed on wing leading edges (LE) and trailing edges (TE) has been used to improve wing response and aircraft maneuverability [6].

During recent years aeronautical research has seen multicontrol surfaces architecture being investigated for different aircraft configurations, such as the Sensorcraft [7,8] and the blended wing body aircraft [9]. In both cases, usage of many control surfaces on a wing aims at improving adaptiveness capability of the wing, to fit more stringent mission requirements, such as high altitude and long endurance (in the case of the Sensorcraft) or high efficiency and, in some cases, very low noise impact (blended wing body). The work

presented in this paper deals with the usage of multicontrol surfaces configuration for dynamic control and, to be more accurate, with modal control: a fast and efficient way to generally obtain some aeroelastic response improvement is strictly based on the capability of shaping structural normal modes [10–12]. The combined usage of multiple control surfaces and active control is hence investigated so as to exploit structural wing deformations and their interaction with external unsteady loads in a beneficial way (resulting in favorable improvements in both performance, load alleviation, and actuation power reduction). The purpose, in fact, is to be able to add damping to two specific wing modes: the first wing bending and wing torsion. Those modes, are, in fact, typically addressed as the cause for inducing flutter on the wing, and the ability to use all leading- and trailing-edge control surfaces installed, appears to be a very promising way of reducing their mutual interaction. This would mean, of course, that the interaction mechanism that may lead to flutter could be moved to higher speed, but, again, this has to be seen as a consequence of controlling wing bending and torsion.

A specific test case will be analyzed here: the aeroelastic demonstrator named X-DIA, designed and built by the authors [13,14] during the European research project named Active Aeroelastic Aircraft Structures (3AS) [15]. The main objective of this demonstrator is the realization of a multipurpose benchmark devoted to measuring, testing, and developing different control laws while using multiple control surfaces. The X-DIA reference aircraft, is an unconventional three-surface airplane, thus featuring a widely extended all-movable canard wing, a forward-swept main wing, and a rear T tail. In particular, two canard configurations have been investigated, backswept and forward swept (with a sweep angle of ± 25 deg), as shown in Fig. 1. This vehicle is a midrange passenger airplane: the cabin can carry up to 80 passengers traveling at a cruise speed of 400 kt at an altitude of 26,250 ft. Some noncommon structural solutions have been adopted, following an idea proposed by Roskam [16], aimed at optimizing fuselage inner volumes and simplifying wing–fuselage connection. In fact, the main wing is placed at the end of the fuselage and is directly connected to the main fuselage rib, to which the landing gear and the T tail are also attached. This solution also allows the pressure bulkhead to be placed right before the same fuselage rib and be efficiently designed. The wing follows a classical stringers and spars solution technique, with ribs distributed along the span. The locations of the main spars along the chord length are 30 and 70%, respectively; fuel tanks are embedded inside the wing, and 30% of the wing span (i.e., the part near the wing tip) is not used by the fuel tanks. The aircraft wings have a sweep angle of -15 deg, and a $+3$-deg dihedral angle. The number of control surfaces, that is, completely movable canard, multiple leading-edge and trailing-edge surfaces, and T-tail surfaces, allows a nontrivial solution for trimming and a combination of control surfaces which could permit efficient static and dynamic control at the same time. For these reasons the X-DIA has been turned into an aeroelastic platform, to develop and study aircraft efficiency improvement by means of active aeroelastic control. This is mainly focused on investigating the achievable aeroelastic improvements that could be gained by the adoption of active control, coupled with a redundant number of control surfaces. Unlike many other jet liners, in fact, the X-DIA is provided with a very slender forward-swept wing, with no motor nacelles or other external (attached) masses. Even if this solution provides many aerodynamic advantages, especially in terms of drag and induced drag, one must also consider that, due to its tiny shape, such a wing might suffer from a sort of overrelaxation of bending and torsional stiffness. The X-DIA (semi) wing is hence equipped with four control surfaces: two of them located on the leading edge, and two of them placed on the trailing edge, for a total of four control surfaces (eight on the complete wing). This solution allows, in fact, each aerodynamic surface to have a double role: while still making it possible to use them to control aircraft maneuvers when properly activated these surfaces also allow sufficient aerodynamic forces to be generated to damp wing normal modes, improve gust response, and to provide enhanced flying comfort for the aircraft. This research has been conducted both numerically and experimentally using a wind-tunnel half-wing model based on the original X-DIA architecture. In the following sections a complete description of the numerical models, experimental setup, and collected results is reported.

II. Wing Model Description

The forward-swept wind-tunnel aeroelastic wing model, also named black wing (since it is entirely made of carbon fabric), is based on the X-DIA wing reference prototype and it has been obtained by using the complete Froude scaling methodology [17], with a geometric scale factor equal to one-tenth. Details about the procedure adopted to realize the model can be found in the literature [18]. The structural solution chosen to build the model is quite traditional and it relies on beams and masses: beams reproducing wing stiffness along the span and masses to reproduce mass effect along the span. A more detailed description of this model will be provided in the following paragraphs.

A. Wind-Tunnel Wing Model Structure

The wing model features a single carbon fabric spar with a hollow cross-section shape. This spar is located at 37% chord span and it has been made up with different numbers of plies on the core section and on the peripheral part of the cross section, with the following lamination sequence: 0/90 deg. The entire main spar has been polymerized in an autoclave by means of the vacuum bag technique. The hollow cross-section spar has been obtained by joining together two omega-shaped spars with structural glue. This wing model presents four control surfaces: two of them are located on the leading edge and the remaining two on the trailing edge, still distributed along the span. Each control surface is connected to the spar through an aluminum alloy rib, properly milled to ensure both enough stiffness and correct hinge axis alignment with respect to the main spar; moreover, each rib has been milled to contain ball bearings to reduce actuation frictions. Aluminum alloy ribs are attached to the main spar by means of structural glue. The names of the four control surfaces are given as leading edge outer (LEO), leading edge inner (LEI), trailing edge outer (TEO), and trailing edge inner (TEI), according to NASA terminology [4]. Leading-edge surfaces are made with styrofoam covered with carbon fiber, whereas the trailing

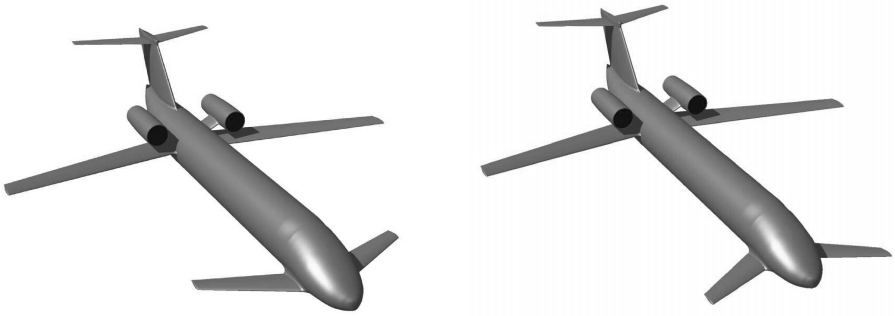

a) Backswept Canard b) Forwardswept Canard

Fig. 1 X-DIA trimetric view.

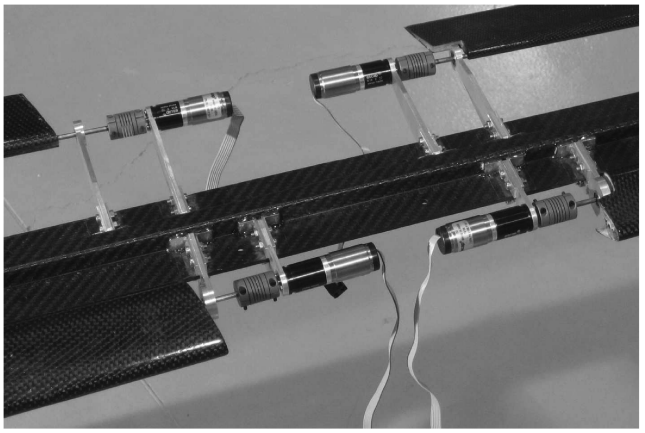

a) Actuators and control surfaces connection, upper view

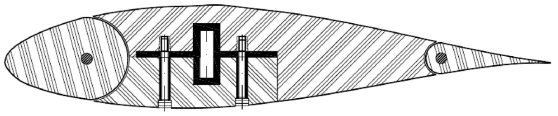

b) Wing model section

Fig. 2 Images of wing model, actuators, and CAD view of aerodynamic sector.

edges are made with balsa wood, also covered with a carbon fiber ply. A steel beam is placed inside each surface and works as a torsion tube. The connection between actuators and surfaces is provided by helical flexible joints. Aerodynamic sectors, made with styrofoam and a prepreg carbon fabric, are used to reproduce the external shape of this wing. These last are connected to the main spar by means of bolts, with a connection system that is not affecting overall wing stiffness distribution (thus, apart from reproducing external shape these sectors also introduce some mass terms and inertia too). Figure 2 shows details of the model. The aeroelastic wing model has been equipped with four independent current controlled electric actuators. These electric brushed motors were chosen to be embedded right inside the wing airfoil thickness. By means of specifically designed current power drivers, these can provide the required torque within the wing model flight envelope. Table 1 briefly summarizes the model wing data, while Table 2 reports its modal properties. Four integrated circuit-piezoelectric (ICP)-monoaxial piezoelectric accelerometers are also embedded directly on the wing and allow measurement of accelerations in two regions of the wing: midspan and wing tip. Location of these devices is graphically shown in Fig. 3. The choice of these four specific points to measure accelerations reflects the availability of volume inside the wing and considering the maximal distance from the wing elastic axis, also increases accelerometer sensitivity in observing wing torsion.

B. Actuators Modeling and Control

To choose the correct actuators, both static and dynamic characteristics must be taken into account: this means evaluating maximum

Table 1 Active wing design data

X-DIA black wing specification		
Wing semispan	1.5	m
Wing surface	0.75	m^2
Wing sweep	15	deg
Wing dihedral	3	deg
LEO span	0.55	m
LEI span	0.52	m
TEO span	0.52	m
TEI span	0.55	m
Total mass	2.4[a]	Kg

[a]Weight data include sensors, cables, and other additional parts.

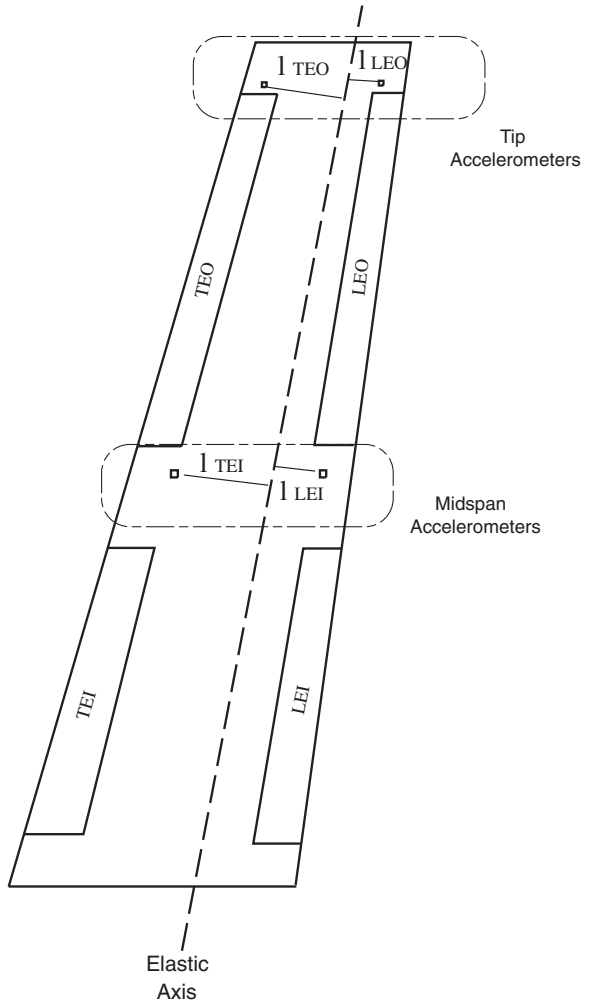

Fig. 3 Model scheme.

continuous torque, bandwidth, and phase lag. While the first allows static positioning granting force balance for all velocity/angle-of-attack envelopes, the other two enable modal control within the requested frequency range. Moreover, two more constraints must be considered: weight, which is an important datum for the correct scaling of a wing model with respect to reference aircraft, that is, full scale X-DIA aircraft, and maximum allowable size, which is limited by airfoil thickness. Trying to reach a good compromise between all these requirements, four electric motors Portescap mod 17N78-210E were selected: Table 3 summarizes some of their characteristics. Maximum torque requirements are met by installing a planetary gear head right on the motor shaft, thus allowing a high reduction ratio while maintaining small size and low weight. A specific choice for gear heads was made: LE motors do have a three stage planetary gear head (with a gear ratio $\tau = 88$), while TE are using a two-stage gear head (where $\tau = 22$). The electromechanical system of equations governing motor dynamic behavior can be usually expressed as

$$L \cdot \frac{\mathrm{d}i}{\mathrm{d}t} = -R \cdot i - K_e \cdot \omega + v \tag{1}$$

Table 2 Modal properties of the black wing

Mode no.	Frequency, Hz	Mode shape
1	9.6	First bending mode
2	15.1	First bending mode—inplane
3	24.7	First torsion mode
4	40.0	First TEO surface bending mode
5	48.0	Second bending mode
6	71.6	Second torsion mode

Table 3 Some characteristics of electric actuators Portescap mod. 17N78-210E

Max continuous current	A	0.37
Max continuous torque	mN/m	4.85
Torque constant	mN/m/A	13.4
Rotor inertia	$kg \cdot m^2$	0.8×10^{-7}
Mechanical time constant	ms	8.0

$$J \cdot \frac{d\omega}{dt} = K_t \cdot i + T_f \tag{2}$$

By solving this system of equations, two poles can be identified: at low frequency, the motor behavior is governed by the mechanical part, while the electric pole resides at higher frequency values, which means that this subsystem can be considered as acting statically, as shown in Fig. 4. Motor bandwidth is then determined by the lower pole, but, to be able to completely evaluate the servoactuator dynamic stability and performances, gear-head inertia and friction, control surface and joint inertia, and kinematic chain compliance contributions must be added. The previously defined term T_f (friction torque), should be expressed as a function of angular velocity if friction is considered to be dependent on angular velocity (this is often done when friction can be measured or particular friction models are developed). In the case under analysis, anyway, this first calculation was only performed to get some useful information directly from the actuators catalogs and data sheet. In fact, most actuator producers do not clearly state the actuators' performances in terms of bandwidth. At first, T_f can be approximated as a constant term. After solving Eqs. (1) and (2), T_f turns out to have no effect on the frequency bandwidth value to be calculated; hence the friction torque has been set to zero. However, once in possession of the actuators, a specific experimental session was carried out to clearly measure the actuators' bandwidth. An experimental identification of mechanical system transfer functions was conducted on a dedicated test bed equipped with the complete kinematic chain and each type of control surface. Measured transfer functions were fitted, adopting a least-square procedure applied to the complete set of measured data, using a polynomial rational function (see Fig. 5 for LEO and TEO control surfaces); although the maximum number of terms is not univocally set, a second-order polynomial representation was chosen whereby giving a physical meaning to the three identified coefficients, that is, starting from the higher term, inertia, damping, and stiffness. During transfer functions acquisition, voltage (and thus current) command was directly fed to the motor and the angular position was measured, bypassing any servoregulator block. The values obtained are summarized in Table 4. Knowledge of the mechanical system, and its modeling, is also crucial to trace closed loop Bode plots and to allow a servoregulator parameters optimization, under a linear and time invariance hypothesis. The main control system structure is based on four independent proportional integral derivative (PID) regulators (as depicted in Fig. 6), each provided with an antiwindup module. These regulators are used to control each wing control surface. Among the many possible solutions which can be adopted to realize antiwindup devices, the mechanism used here, as presented in Fig. 7, works by subtracting a quantity equal to saturation from the error line. This solution improves functionality of the PID regulator even when working in extreme conditions (which were never matched during the wind-tunnel experience presented here). Each regulator has been modified by adding a second derivative feedback to increase motor response and for this reason will be later referred to as PID_2: the number of tunable gains hence rises to four (proportional, integral, first, and second derivatives). Gain setting and optimization have been determined experimentally for each wing control surface. Experimental data are shown in Figs. 8 and 9: here, resulting Bode plots referred to as LEO and TEO actuation ensembles (thus including actuator and control surface) are presented. Table 5 is the result of the combined usage of the previously mentioned PID_2 and of the mechanical system that was experimentally identified. Moreover, as in Table 5, it can be seen that some poles have ξ values below 1. These poles are oscillating and this is only because of the mechanical part of the dynamic system. In fact, it can be seen that the servoactuators bandwidth is about 40 Hz when dealing with the leading-edge control surface and 90 Hz when dealing with the trailing-edge ones, which have lower gear-head inertia values: the former have a filtering action beyond 40 Hz on higher frequency structural modes, like second bending and second torsional ones. Again, in Figs. 8 and 9, magnitude overshooting is due to the oscillating poles. It is sometimes common practice to use a preshaper, that is, a device which literally cancels oscillating pole dynamics, but this requires a prior knowledge of the poles' placements of the system in closed loop. In this case, anyway, the addition of aerodynamics increases difficulties in canceling the desired poles, as these do vary according to flight velocity. Therefore, the preshaper device has not been used. Finally, the addition of a planetary gear head affects actuator dynamics, and to be more specific, the bigger the gear ratio of the gear head, the more is its influence on poles frequency. Anyway, in the present case, gear heads are quite compact (this means that inertial increase is partially compensated by a stiffening action of the precompressed gears installed on each planetary stage); thus the gears are only slightly affecting actuation dynamics. The most critical servoactuator is located on LEI and has a resonance frequency of 18 Hz. In fact, due to its volume and mass, the LEI control surface is characterized by the highest inertia value. Its actuator presents a phase lag near to the first torsional mode, which is about 50 deg, but still grants enough margin for the subsequent use in the active control design.

C. Aeroservoelastic (ASE) Wing Modeling

The numerical aeroservoelastic model which, as previously mentioned, is the basis of the aeroelastic wind-tunnel model, was realized using MSC/NASTRAN and in-house developed MATLAB procedures. At first, a structural model was generated using beam and concentrated mass elements; then it was updated on the basis of ground vibration testing results, carried out with the hammer technique and reported in Table 2, using LMS CADA-X software. The first three normal modes of this model are shown in Fig. 10.

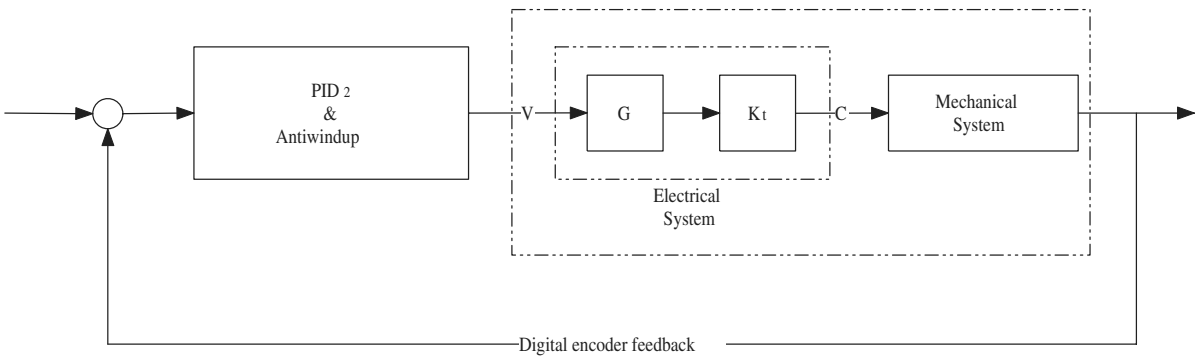

Fig. 4 Single surface feedback conceptual scheme.

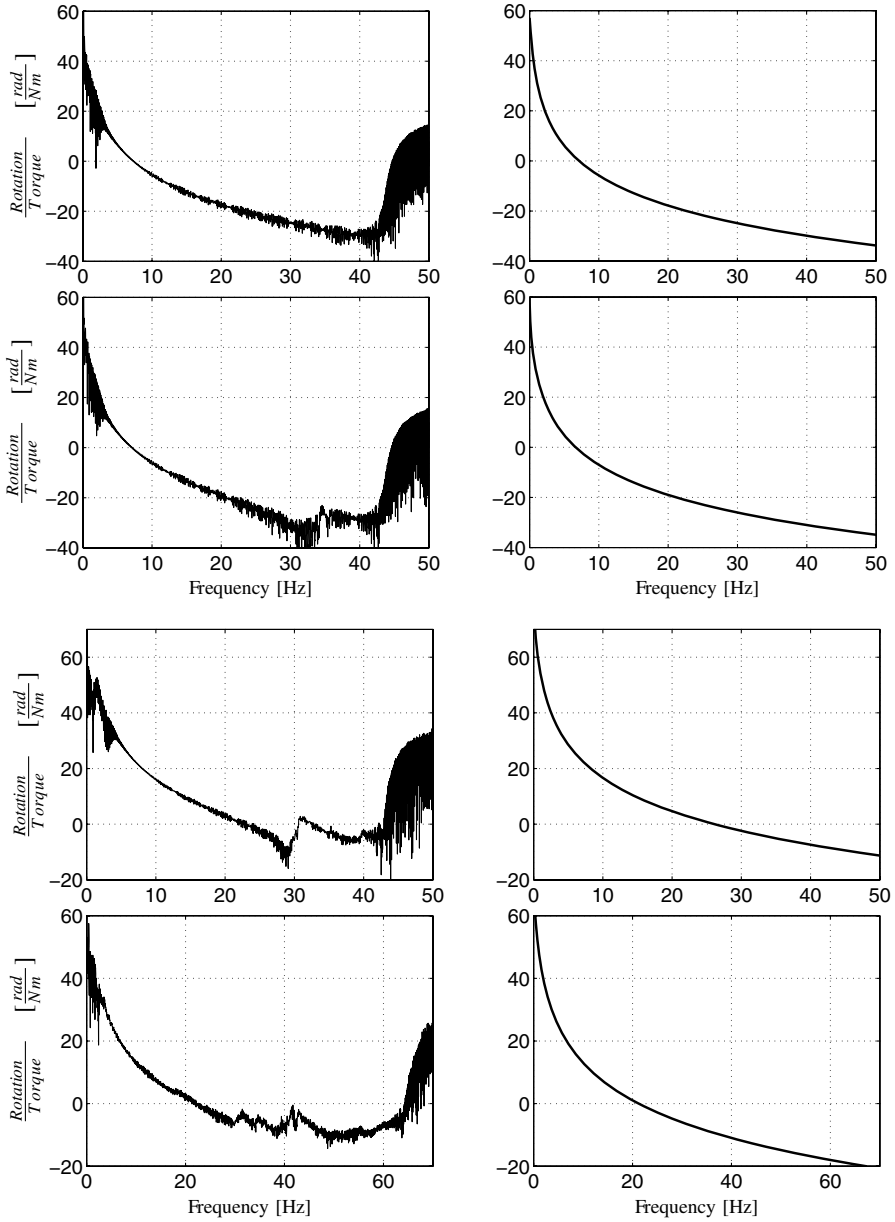

Fig. 5 Measured and identified mechanical system transfer functions, from top to bottom: LEO and TEO.

The aerodynamic model was developed by means of the MSC/NASTRAN doublet lattice method (DLM). Finally, structural and aerodynamic models were processed by means of an in-house developed code, and subsequently translated into a state-space aeroelastic model. As a result of this technique a state-space dynamic system of equations which, when given the modal structural degrees of freedom as input, produces the aerodynamic load as output. This system can be connected in feedback to the one which represents structural modal response to obtain a complete time domain aeroelastic model. The detailed procedure, briefly recalled here, can be found in a previous paper [19]; the most relevant steps will be reported next.

Table 4 Coefficients for identified mechanical systems

System	Inertia, kg · m^2	Damping, N · m · s	Stiffness, N · m
LEI	5.73×10^{-4}	4.04×10^{-3}	1.04×10^{-3}
LEO	4.87×10^{-4}	2.38×10^{-3}	1.39×10^{-3}
TEI	5.09×10^{-5}	4.31×10^{-4}	2.11×10^{-4}
TEO	3.70×10^{-5}	2.28×10^{-4}	1.13×10^{-4}

The current practice adopted to represent unsteady aerodynamic forces is based on the rational approximation of aerodynamic transfer functions generally available in the frequency domain, since computed small structural motions as solutions of integrodifferential equations are related to harmonic boundary domain oscillation.

Various formulations can be found in the literature dealing with the rational approximation of aerodynamic transfer function [20–25]; in any case, the common starting point is knowing the generalized aerodynamic forces in the following form:

$$\mathbf{f} = \mathbf{H}_{am}(k, M_\infty) \cdot \mathbf{q} + \mathbf{H}_{ag}(k, M_\infty) \cdot \frac{V_g}{V_\infty} \tag{3}$$

Here, $\mathbf{H}_{am}(k, M_\infty)$ and $\mathbf{H}_{ag}(k, M_\infty)$ are the unsteady aerodynamic and gust frequency response matrices. Ignoring any gust contribution, matrix $\mathbf{H}_{am}$, which only here will be called $\mathbf{H}_a$, can be obtained by the following polynomial approximations:

$$\mathbf{H}_a(p) = \mathbf{D}_0 + \mathbf{D}_1 p + \mathbf{D}_2 p^2 + \mathbf{C}(p\mathbf{I} - \mathbf{A})^{-1}\mathbf{B} \tag{4}$$

where $\mathbf{A}$, $\mathbf{B}$, $\mathbf{C}$, and $\mathbf{D}_i$ are the state-space aerodynamic matrices. Roger [21] proposed to approximate those matrices as

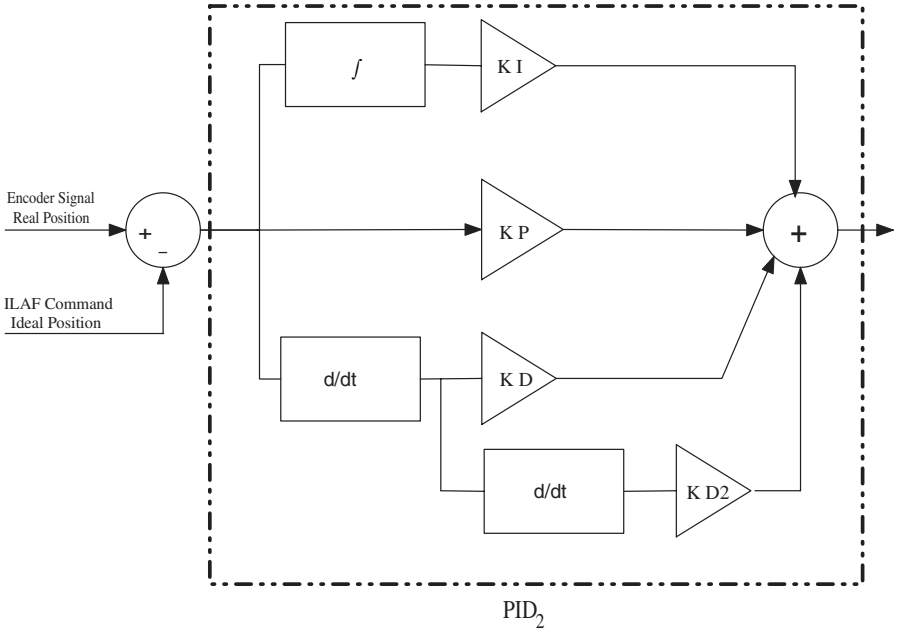

Fig. 6 $\mathbf{PID_2}$ conceptual scheme.

$$\mathbf{H}_a(p) \simeq \mathbf{D}_0 + \mathbf{D}_1 p + \mathbf{D}_2 p^2 + \sum_{i=1}^{m} \frac{p}{p+\beta_i}\mathbf{E}_i \tag{5}$$

where poles $-\beta_i$ are prescribed by the user in the range of interest of p, and where their real part is negative to ensure the stability of the dynamic system. All the coefficients are evaluated using a least-square technique on each individual term. The resulting model for the aerodynamic generalized forces has a $m \cdot n$ dimension, where n is the number of structural generalized degrees of freedom. Roger's technique is straightforward, robust, easy to implement, and inexpensive in terms of computational burden. However, it means significantly increasing the states number to improve accuracy: the addition of a new pole means incrementing the state number by n. In any case, Roger's technique is not the only way to obtain reduced order models: the literature offers many examples of techniques (see, for instance, Karpel [22], but also Morino et al. [25], who proposes a sort of multipoint Padé approximation) that makes good results possible, with quite a reasonable computational effort, especially with today's computers. The procedure here adopted is based on coupling the classical Roger's approach with an optimization procedure for pole positioning to minimize the local relative error. Then, a balanced truncation reduction methodology [25,26] was applied to recover small compact models for the aerodynamic generalized forces. Finally, to improve the quality of the reduced order model in the low frequency range, an exact fit of the real part and of the slope of the aerodynamic forces transfer function at zero reduced frequency was enforced by applying a dynamic residualization of fast system dynamics [27]. More details on the procedure summarized here may be found in [28].

After determining the state-space aerodynamic system [Eq. (5)], a set of state-space equations describing the aeroelastic system model were drawn up and have the form [Eq. (6)]

$$\dot{\mathbf{x}} = A\mathbf{x} + B\mathbf{u}, \qquad \mathbf{y} = C\mathbf{x} + D\mathbf{u} \tag{6}$$

Each generalized structural degree of freedom was necessarily represented by two states $\mathbf{q}$ and $\mathbf{r}$ (where $\mathbf{q}$ represents the generalized degree of freedom and $\mathbf{r}$ the virtual state) so that the aeroelastic system model could be described as follows [Eq. (7)]:

$$E_{ae}\dot{\mathbf{x}}_{ae} = A_{ae}\mathbf{x}_{ae} + B_{ae}\mathbf{f} \tag{7}$$

The described terms E_{ae}, A_{ae}, and B_{ae} are defined as follows:

$$E_{ae} = \begin{bmatrix} M_{ae} & 0 & 0 \\ 0 & I & 0 \\ 0 & 0 & I \end{bmatrix}, \qquad A_{ae} = \begin{bmatrix} -C_{ae} & I & 0 \\ -K_{ae} & 0 & qC_a \\ (V_\infty/c)B_a & 0 & (V_\infty/c)A_a \end{bmatrix}$$

$$B_{ae} = \begin{bmatrix} 0 \\ I \\ 0 \end{bmatrix} \tag{8}$$

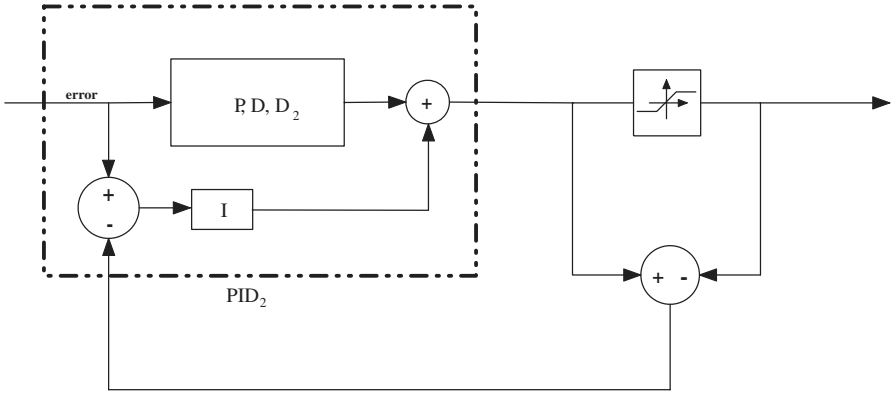

Fig. 7 Antiwindup conceptual scheme.

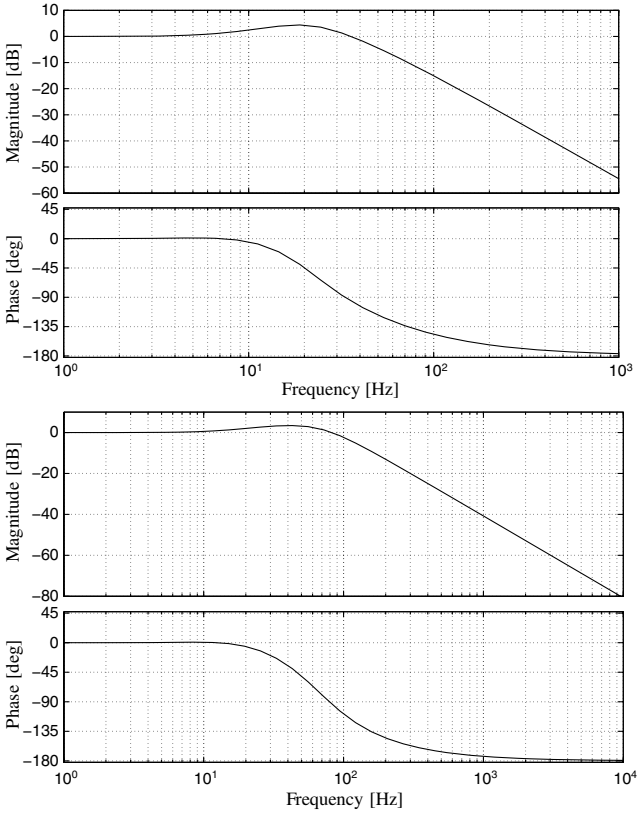

Fig. 8 Bode diagrams, from top to bottom: LEO and TEO—experimental.

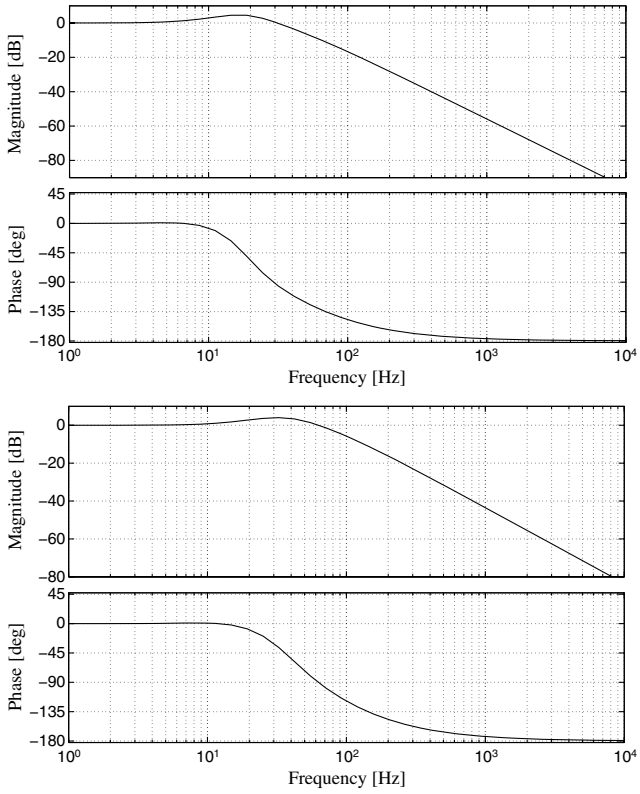

Fig. 9 Bode diagrams, from top to bottom: LEI and TEI—experimental.

To build the matrices above, M_{ae}, C_{ae}, and K_{ae} must also be defined in the following way:

$$M_{ae} = M_s - q(c/V_\infty)^2 D_2 \tag{9}$$

$$C_{ae} = C_s - q(c/V_\infty)^2 D_1 \tag{10}$$

$$K_{ae} = K_s - qD_0 \tag{11}$$

Moreover, A_a and B_a and C_a are known once the fourth term of Rogers approximation presented in Eq. (5) is solved. Finally, $\mathbf{x}_{ae}$ is defined as follows:

$$\mathbf{x}_{ae} = \begin{Bmatrix} \{\delta_i\} \\ \mathbf{q} \\ \{\delta_{ir}\} \\ \mathbf{r} \\ \mathbf{x}_a \end{Bmatrix} \tag{12}$$

where $\{\delta_i\}$ are control surfaces rotation angles (δ_{LEO}, δ_{TEO}, δ_{LEI}, and δ_{TEI}, respectively), whereas the virtual state vector $\mathbf{r}$ is defined by

$$\mathbf{r} = M_s\dot{\mathbf{q}} + C_s\mathbf{q} - q(c/V_\infty)^2 D_2\dot{\mathbf{q}} - q(c/V_\infty)D_1\mathbf{q} \tag{13}$$

It is still possible to use the state system to compute the accelerometer measurements output that will be used as direct feedback of the active control system. These are computed by the modal participation of nodes placed in correspondence to the accelerometers along the desired direction. The last step of the ASE model formulation was obtained by introducing the actuator's dynamic model into aeroelastic equations. Each servoactuator, driven by the required position of the control surface δ_c, generates as output the corresponding hinge moment acting on the structure. Considering the control chain as infinitely stiff, the dynamic behavior of all four control surfaces on the wing can be expressed as

$$\{\delta_i\} = [H_\delta]\{\delta_{c,i}\} \tag{14}$$

The numerical ASE model was then used to develop the modal control scheme and to design the hardware for wind-tunnel testing.

III. Control System

The control system created and installed is primarily devoted to increasing wing stability by means of modal control. Four aerodynamic control surfaces are moved with a control law which deflects them to augment or decrease wing camber with the aim of producing a variable lift distribution capable of damping bending and torsion modes. The entire control system can be regarded as a reorganization of the identical location of acceleration and forces (ILAF) concept [12]; thus a sort of discrete colocated control already applied to the aeroelastic demonstrator during the 3AS project [18,29] is here slightly modified in terms of actuation law to better fit the wing modal control. As previously mentioned, each control surface is moved by a single actuator, and each actuator is regulated by a specifically tuned PID_2. Deflection of each control surface, requested by the ILAF control law, is summed to error line and sent to each actuator PID_2 regulator, thus closing the feedback loop, as shown in the conceptual scheme reported in Fig. 11. In the following lines, a detailed description of control implementation and tuning is given.

A. Modal Control Design Framework

The methodology adopted to design and improve the modal control system follows some steps already presented by the authors in some previous works [19,30]: usage of state-space reduced order models, connected in feedback with some MATLAB-Simulink models representing the control system. By means of environments such as Linux-RTAI and RTAI-LAB [31] a complete time domain simulation can be run, and a simple substitution of the states space model with the wind-tunnel experiment can allow the use of the same

Table 5 Closed loop poles of LEI, LEO, TEI, and TEO systems

LEI		LEO		TEI		TEO	
f, Hz	ξ	f, Hz	ξ	f, Hz	ξ	f, Hz	ξ
5.05	1.00	5.10	1.00	8.68	1.00	8.93	1.00
18.45	0.55	21.53	0.62	37.67	0.68	33.41	1.00
49.21	1.00	42.30	1.00	80.34	1.00	67.86	1.00
90.40	1.00	90.40	1.00	147.81	1.00	146.41	1.00
91.02	1.00	91.02	1.00	159.21	1.00	159.21	1.00

personal computer and hardware for both simulation and real testing. Sections III.B and III.C will provide explanations about the design and tuning of this control system. The entire system has been designed for a bandwidth of 30 Hz, so as to control first bending and first torsion modes, and later optimized for a speed of 30 m/s: this speed was chosen because from preliminary simulations and wind-tunnel tests, the aerodynamics turned out to be already very effective. Indeed, the wing tested here uses a NACA airfoil, which commonly operates at higher Reynolds numbers; moreover, it must also be considered that the model is not an aerodynamic wind-tunnel model, but an aeroelastic one, that is to say, showing the presence of gaps, windows, and features which can roughly be addressed as aerodynamic. Even in this case, however, even at 30 m/s, small deflections of all control surfaces appeared to be highly capable of affecting wing bending and torsion.

B. Modal Bending and Torsion Velocities

The main feature of the ILAF control system is represented by the fact that the deflection of a single control surface is forced to be proportional to structural velocity evaluated in the same structural points where control forces are applied (thus, a very simple and straightforward concept). In this specific case, the wing has four different control surfaces, which are working in different locations on the wing and in different aerodynamic fields. Application of the colocated ILAF concept on the X-DIA black wing followed a sort of different implementation. The wing is actually divided into two active camber strips (inner and outer strips) that can work independently, where leading- and trailing-edge surfaces can be used together in synchronous mode, with independent differential deflection. This implies that while the inner strip is moving LE and TE together in synchronous mode, the outer strip is also deflecting LE and TE, still in synchronous mode, but with deflections independent of the inner strip. To build the control system, the control signal had to be first isolated: keeping in mind that the main objective is to control wing bending and torsion modes, a structural velocity directly related to these two modes can be obtained by evaluating acceleration on the fixed part of LE and TE for each wing active strip (inner and outer) as follows:

$$\begin{Bmatrix} \ddot{b}_{\text{in}} \\ \ddot{\theta}_{\text{in}} \\ \ddot{b}_{\text{out}} \\ \ddot{\theta}_{\text{out}} \end{Bmatrix} = \begin{bmatrix} \frac{l_{\text{TEI}}}{l_{\text{LEI}}+l_{\text{TEI}}} & \frac{l_{\text{LEI}}}{l_{\text{LEI}}+l_{\text{TEI}}} & 0 & 0 \\ \frac{1}{l_{\text{LEI}}+l_{\text{TEI}}} & -\frac{1}{l_{\text{LEI}}+l_{\text{TEI}}} & 0 & 0 \\ 0 & 0 & \frac{l_{\text{TEO}}}{l_{\text{LEO}}+l_{\text{TEO}}} & \frac{l_{\text{LEO}}}{l_{\text{LEO}}+l_{\text{TEO}}} \\ 0 & 0 & \frac{1}{l_{\text{LEO}}+l_{\text{TEO}}} & -\frac{1}{l_{\text{LEO}}+l_{\text{TEO}}} \end{bmatrix} \begin{Bmatrix} \ddot{Z}_{\text{LEI}} \\ \ddot{Z}_{\text{TEI}} \\ \ddot{Z}_{\text{LEO}} \\ \ddot{Z}_{\text{TEO}} \end{Bmatrix} \tag{15}$$

In Eq. (15), terms $\ddot{b}_{\text{in}}$, $\ddot{b}_{\text{out}}$, $\ddot{\theta}_{\text{in}}$, and $\ddot{\theta}_{\text{out}}$ represent bending and torsional accelerations of inboard and outboard wing strips. These quantities, during the design of the control system, are calculated from the state-space reduced order model: according to Eq. (15), these are nonetheless evaluated as a weighted mean of structural accelerations of four specific points (each one of these points is represented in the finite element model (FEM) model shown in Figs. 10, with a specific node). Again, when operating on the wind-tunnel model, bending and torsion accelerations are immediately computed from a weighted mean of accelerometric signals. These accelerometers are therefore located in the same positions as the previously mentioned specific points. Figure 3 recalls the location of these points, and also the geometric definition of the four quantities named, respectively, l_{LEI}, l_{LEO}, l_{TEI}, and l_{TEO}. Because ILAF logic requires the use of structural velocities, these last quantities are obtained from the previously listed piezoelectric accelerometers located on the wing. Structural velocity is thus obtained from structural acceleration using pseudointegration: this technique, which is usually adopted within experimental tests [32], was chosen to prevent and avoid long term drifts and possible saturations of the integrator. Pseudointegration, in fact, is commonly performed by using the following transfer function as integrator:

$$I(s) = \frac{\omega_f^2 s}{s^2 + 2\xi_f \omega_f s + \omega_f^2} \tag{16}$$

This approximation generates a device that works essentially as a real integrator only after a specified frequency (hence acting like a high pass filter, with respect to integration). During the design and the experimental validation of the wing control system, proper choice of ω_f and ξ_f were made to ensure enough separation between the wing lowest mode and the short period motion of the aircraft. Bending and torsion structural velocities are computed independently for each wing active strip.

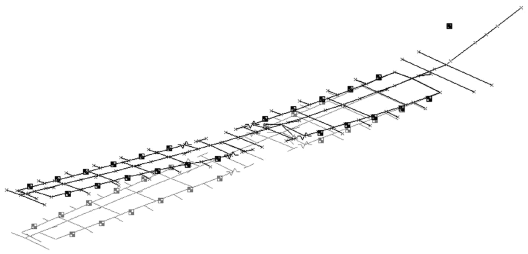

a) First bending mode

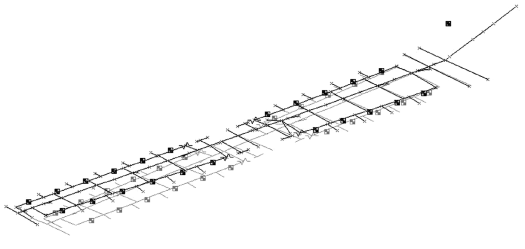

b) In-Plane bending mode

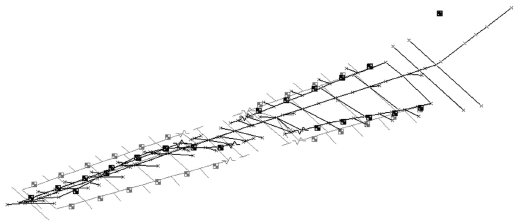

c) First torsion mode

Fig. 10 The first three mode shapes of the wing model.

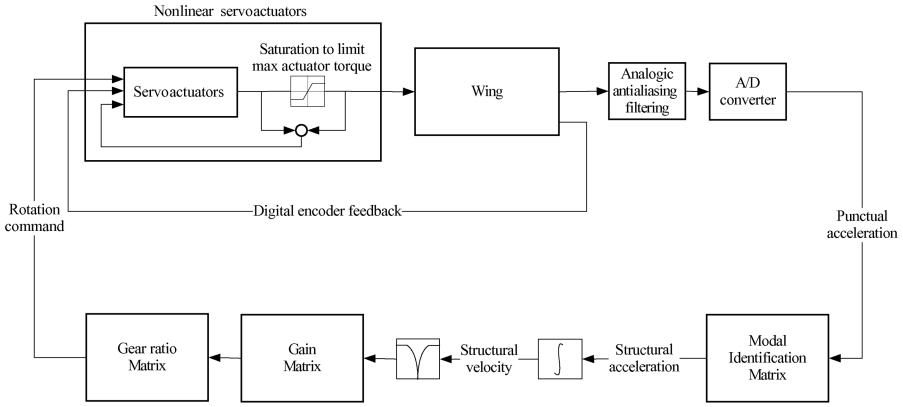

Fig. 11 Control scheme.

C. Gear Ratios and Root Loci

Once control signals (i.e., wing bending and torsion structural velocities) have been determined, these signals have to be processed to control LE and TE surface deflection. Wing leading and trailing edges can be differentially deflected to produce a sort of pure lift (this implies a clockwise LE rotation and a clockwise TE rotation) when bending occurs or a pure aerodynamic moment, as shown in Fig. 12 (this implies a counterclockwise LE rotation and a clockwise TE rotation) when in the presence of wing torsion. Usage of the term "pure" is to point out that wing camber variation is performed with the intention of generating either the highest possible lift force, while minimizing aerodynamic moment, or the highest possible amount of aerodynamic moment, while minimizing lift force. The correspondence between control signal and deflection is performed in the following way: when bending or torsion occurs, a fixed gear ratio (which, according to the ILAF concept, is directly proportional to structural velocity) states the correct deflection of leading and trailing edges at a single wing station (either inner or outer strip). The gear ratio is multiplied by a sensitivity gain matrix that can easily tune control system aggressiveness or exclude any surface from control action, that is,

$$\begin{Bmatrix} \delta_{\mathrm{LEO}} \\ \delta_{\mathrm{TEO}} \\ \delta_{\mathrm{LEI}} \\ \delta_{\mathrm{TEI}} \end{Bmatrix} = \begin{bmatrix} 0 & 0 & GR_{\mathrm{lebo}} & GR_{\mathrm{leto}} \\ 0 & 0 & GR_{\mathrm{tebo}} & GR_{\mathrm{teto}} \\ GR_{\mathrm{lebi}} & GR_{\mathrm{leti}} & 0 & 0 \\ GR_{\mathrm{tebi}} & GR_{\mathrm{teti}} & 0 & 0 \end{bmatrix} \times \begin{bmatrix} G_{\mathrm{bin}} & 0 & 0 & 0 \\ 0 & G_{\mathrm{tin}} & 0 & 0 \\ 0 & 0 & G_{\mathrm{bout}} & 0 \\ 0 & 0 & 0 & G_{\mathrm{tout}} \end{bmatrix} \begin{Bmatrix} \dot{b}_{\mathrm{in}} \\ \dot{\theta}_{\mathrm{in}} \\ \dot{b}_{\mathrm{out}} \\ \dot{\theta}_{\mathrm{out}} \end{Bmatrix} \tag{17}$$

where b_{in}, t_{in}, b_{out}, and t_{out} mean bending and torsion, inboard and outboard, respectively. Gear-ratio values, together with control surface gains, have been evaluated through numerical simulations, just with a simple observation of closed loop root locus. The steps taken to get to the final set of gains and ratios were two: at first every single control surface was tuned independently and at a second stage, all four control surfaces were activated together. Root loci diagrams, reported in Figs. 13 and 14, were used during both stages of control system design and tuning: when dealing independently with control surfaces, four single-input/single-output (SISO) systems are produced, and poles are diagrammed by varying gear ratios. Gear ratios

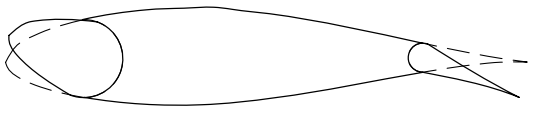

a) Bending control

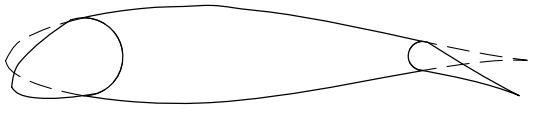

b) Torsion control

Fig. 12 Variable camber mechanism for modal control.

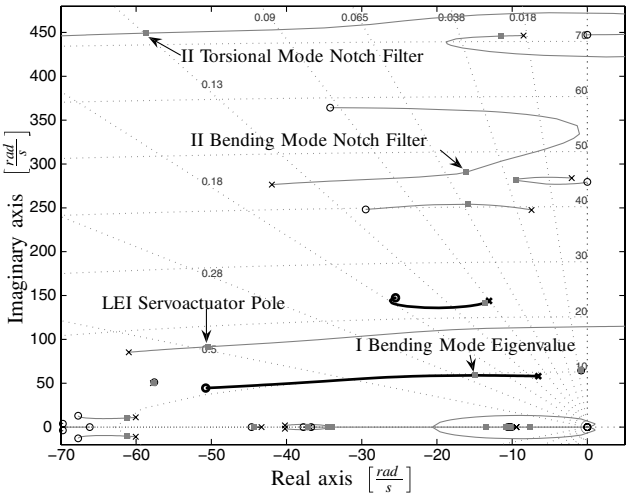

a) Bending

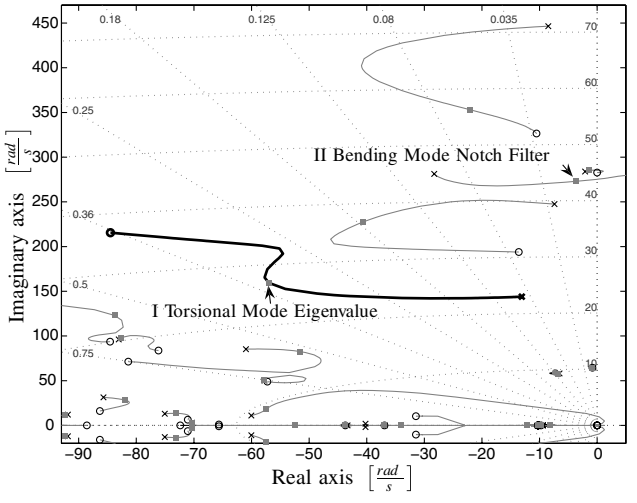

b) Torsion

Fig. 13 Inboard strip: root locus.

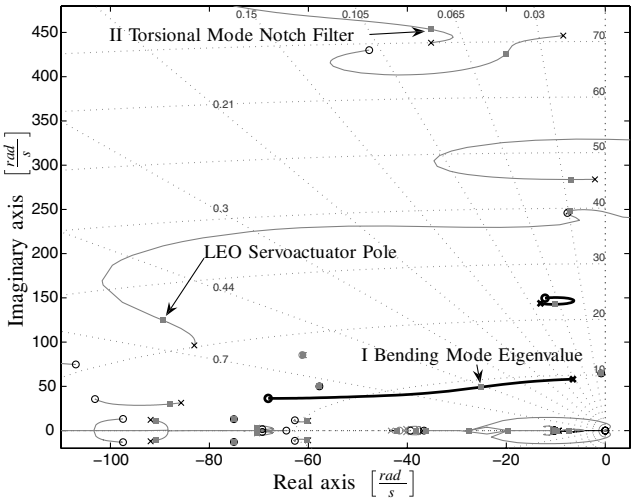

a) Bending

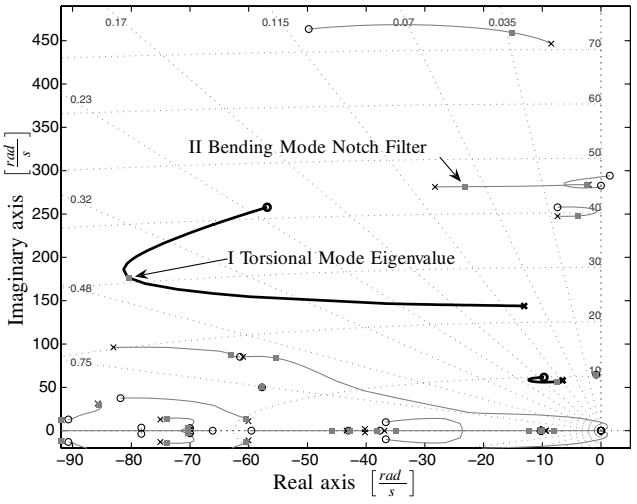

b) Torsion

Fig. 14 Outboard strip: root locus.

are chosen to get the best damping of the selected mode, while keeping the maximum frequency separation between this mode and its complementary, for example, outboard bending and outboard torsion modes. Gains are chosen at a second step: in this case, the choice is made under the constraint of getting maximum system damping, while keeping system global stability. The gear ratios and gains resulting after this first step are reported in the following:

$$\begin{Bmatrix} \delta_{\text{LEO}} \\ \delta_{\text{TEO}} \\ \delta_{\text{LEI}} \\ \delta_{\text{TEI}} \end{Bmatrix} = \begin{bmatrix} 0 & 0 & -0.7 & 0.24 \\ 0 & 0 & 0.3 & 0.76 \\ -0.6 & 0.0 & 0 & 0 \\ 0.4 & 1.0 & 0 & 0 \end{bmatrix} \times \begin{bmatrix} 18.8 & 0 & 0 & 0 \\ 0 & 0.31 & 0 & 0 \\ 0 & 0 & 1.9 & 0 \\ 0 & 0 & 0 & 0.07 \end{bmatrix} \begin{Bmatrix} \dot{b}_{\text{in}} \\ \dot{\theta}_{\text{in}} \\ \dot{b}_{\text{out}} \\ \dot{\theta}_{\text{out}} \end{Bmatrix} \tag{18}$$

After this first iteration, another iteration took place, this time working with multiple-input/multiple-output (MIMO) systems: in this case, gear ratios are kept unchanged, because these terms are directly dependent upon stability derivatives, while control surface gains can be still optimized. Results obtained are very similar to those previously mentioned, except when dealing with bending: here it seems that there is no limit at all to the gain value, thus the limit is represented by the maximum torque provided by the actuators. On the other hand, in the case of torsion mode, an optimum value is reached and this does not depend on actuator maximum torque. Gear ratios and gains obtained in this way were used for wind-tunnel testing. By looking at the root-locus diagram, two notch filters can be identified: they have been introduced between pseudointegrators and close-loop gains to avoid any spill-over effects on second bending and torsional modes, which are, anyway, outside target control bandwidth. The final optimized values for gear ratios and gains to be implemented during experimental validation are reported in the following lines, where gear ratios are normalized to a unitary sum: in this way making gains is independent of aerodynamic load distribution while their signs are dependent on the adopted convention:

$$\begin{Bmatrix} \delta_{\text{LEO}} \\ \delta_{\text{TEO}} \\ \delta_{\text{LEI}} \\ \delta_{\text{TEI}} \end{Bmatrix} = \begin{bmatrix} 0 & 0 & -0.7 & 0.24 \\ 0 & 0 & 0.3 & 0.76 \\ -0.6 & 0.0 & 0 & 0 \\ 0.4 & 1.0 & 0 & 0 \end{bmatrix} \times \begin{bmatrix} 4.48 & 0 & 0 & 0 \\ 0 & 0.1 & 0 & 0 \\ 0 & 0 & 0.422 & 0 \\ 0 & 0 & 0 & 0.07 \end{bmatrix} \begin{Bmatrix} \dot{b}_{\text{in}} \\ \dot{\theta}_{\text{in}} \\ \dot{b}_{\text{out}} \\ \dot{\theta}_{\text{out}} \end{Bmatrix} \tag{19}$$

Looking at the final values of the gear ratios, it appears that leading-edge control surface authority dominates the torsional control, whereas the trailing-edge control surfaces are the most effective for controlling bending.

The block diagram reported in Fig. 11 shows the final control architecture. It is possible to see a nonlinear saturation block, introduced into the servoactuators control block, so as to limit the maximum current sent to actuators during control. This limits maximum torque to a value of 0.4 N · m for LEO and LEI, and 0.1 N · m for TEO and TEI control surfaces, respectively. The electric motor adopted here, if properly coupled to an appropriate current driver, is capable of a higher maximum torque equal to 1 N · m (which is actually the maximum torque allowed by the planetary gear head): the applied limits were chosen to guarantee the requested frequency bandwidth and to satisfy the maximum allowable current obtainable by the amplifier circuit. Finally, as already mentioned, a notch filter was introduced into the control loop so as to eliminate spillover effects caused by uncontrolled second bending and torsion modes.

IV. Experimental Setup

The experimental activity related to the X-DIA black wing took place at the Politecnico di Milano—Department of Aerospace Engineering over a period of several months, starting in February 2006. The wind tunnel used is a closed-circuit type, with a rectangular cross-section test chamber measuring 1.5 m high, 1 m wide, and 3 m long. Wind speed can rise up to a maximum value of 55 m/s. The wing has been installed in the vertical position, right in the middle of the test chamber. Figure 15 shows the wing status during the test sessions. The installation inside the test chamber was realized by attaching the wing itself to a balance, by means of a device that replicates a connection to the fuselage, and also allows angle-of-attack variation. Several tests were initially run to check model installation and realization. Then, static aerodynamic tests were run at different speeds and angles of attack, to find out possible actuator limits, and overall wing behavior. Data obtained from the wind-tunnel balance were then compared to MSC/NASTRAN. As the model demonstrated good functionality, excitation was introduced and response tests were run.

The model is provided with four monoaxial piezoelectric accelerometers, placed as shown in Fig. 3. Signals are processed by a multichannel signal conditioner, and from there are sent to a

a) Side view

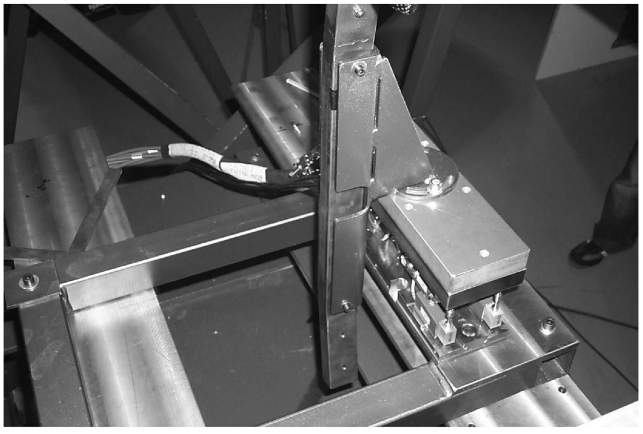

b) Angle-of-attack variation mechanism

Fig. 15 Wind-tunnel wing installation.

multichannel analog low-pass filter (100-Hz cutoff frequency), to avoid possible aliasing problems. The wing is equipped with four electric actuators, with a different planetary gear head, depending on their location. As previously discussed, the choice was made on the basis of the maximum torque requested during the deflection of each surface at the maximum wind-tunnel speed, and in the worst condition possible. On each actuator an incremental encoder is directly connected to the motor axis. Because of the size of this device, the maximum number of lines available is 16, but thanks to the planetary reduction gear ratio and also to a quad sampling technique the number of lines can be improved to a maximum of 3502 and 1408 for LE and TE, respectively. An additional sensor is represented by the wind-tunnel balance. When testing static wing performances, the wind-tunnel balance signal is read as any other signal and can be processed in real time at the fixed frequency of 1 kHz, but when flutter and any other dynamic testing is run, the balance is substituted by an aluminum alloy block for the sake of safety. All control signals and accelerometers are generated or read by a single PC running RTAI-Linux equipped with NI 6036, NI 6713, and Advantech 1784 i/o boards. Drivers for the NI input–output devices were already available at Comedi, whereas devices for digital encoders were created for this specific purpose. The command signal is generated first by Simulink software and then sent from the output board to a rack containing specifically built power drivers to actuate all actuators in current mode. The scheme adopted for this device is a classical Howland type, and it has been realized ad hoc for the experiment by the authors.

V. Wind-Tunnel Results

The test campaign carried out in the wind tunnel was mainly focused on three different aspects. The ASE model was tuned to match the aeroelastic responses against the ones predicted by the numerical ASE model. Flutter identification was then performed and finally the performance of the ILAF-based modal control was evaluated. In the following sections all these issues are described in detail.

A. Aeroservoelastic Model Tuning

The first wind-tunnel testing stage was devoted to identifying wing loads and response, measured by means of an aerodynamic balance connected to the main spar and by the accelerometers located over the wing aimed at matching numerical and experimental aeroelastic responses, to realize a numerical state-space model which could allow the creation of the high fidelity numerical simulator needed for developing control laws. During the ASE model generation, explained in the previous section, the updated FEM structural numerical model, together with the DLM aerodynamics, were processed and translated into a state-space model. The predicted aeroelastic responses were then compared to ones actually measured in the wind tunnel. Special attention was devoted to control surfaces effectiveness. In fact, a numerical model like DLM usually overestimates the aerodynamic efficiency of control surfaces due to the low Reynolds number typical of wind-tunnel testing and, mainly, due to the impossibility to model by DLM all the gaps between aerodynamic sectors and control surfaces. There are many empirical possibilities to correct the FEM ASE in order to match numerical and experimentally measured aeroelastic characteristics, for example, reduction of wing surface, air density scaling, panel efficiency scaling, and much more. When updating an aeroelastic model, based on FEM and DLM, one can decide to work both on structure and aerodynamics. Structural mesh updating was performed, using a commercial software produced by LMS, named CADA-X. This software updates FEM element properties to maximize matching between FEM model normal modes and real wing measured normal modes. Once this first update was performed, the remaining tuning was performed manually on the generalized aerodynamic force matrix $\mathbf{H}_{am}$. Control surface hinge moment derivatives were scaled: in this case, $\mathbf{H}_{am}$ columns connected to the generalized mode depicting each leading-edge control surface rotation were scaled of a proper quantity. This operation has the effect of tuning leading-edge hinge moment coefficients with respect to available experimental data. A better improvement was also produced by slightly scaling air density. The combination of these two updates leads to the generation of an aeroelastic model which might not be statically fully correlated, but whose overall behavior matches the measured dynamics well. Figure 16 shows a comparison among control surface effectiveness before and after the updating procedure. The final state-space model has been used during the process of design and optimization of the controller by means of a MATLAB–Simulink environment.

B. Flutter Identification

Before starting to investigate the modal control effectiveness, an experimental wing flutter identification was performed. The wing was excited by using the TEO control surface driven by a frequency sweep in the range 5–30 Hz with an amplitude of 2 deg where

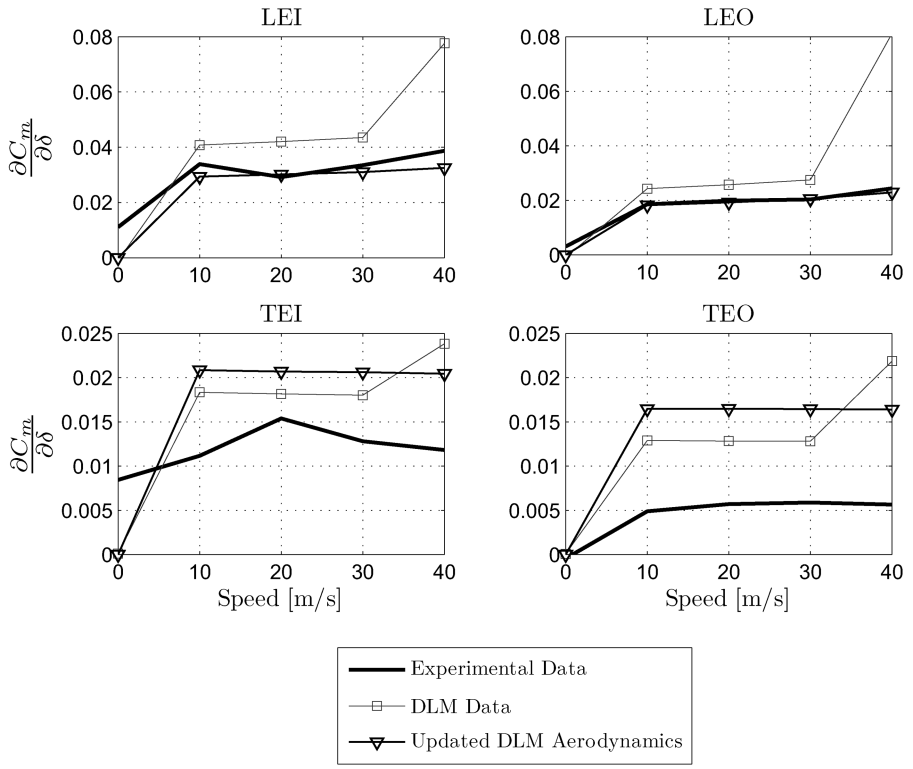

Fig. 16 Hinge moment control surface coefficients before and after updating.

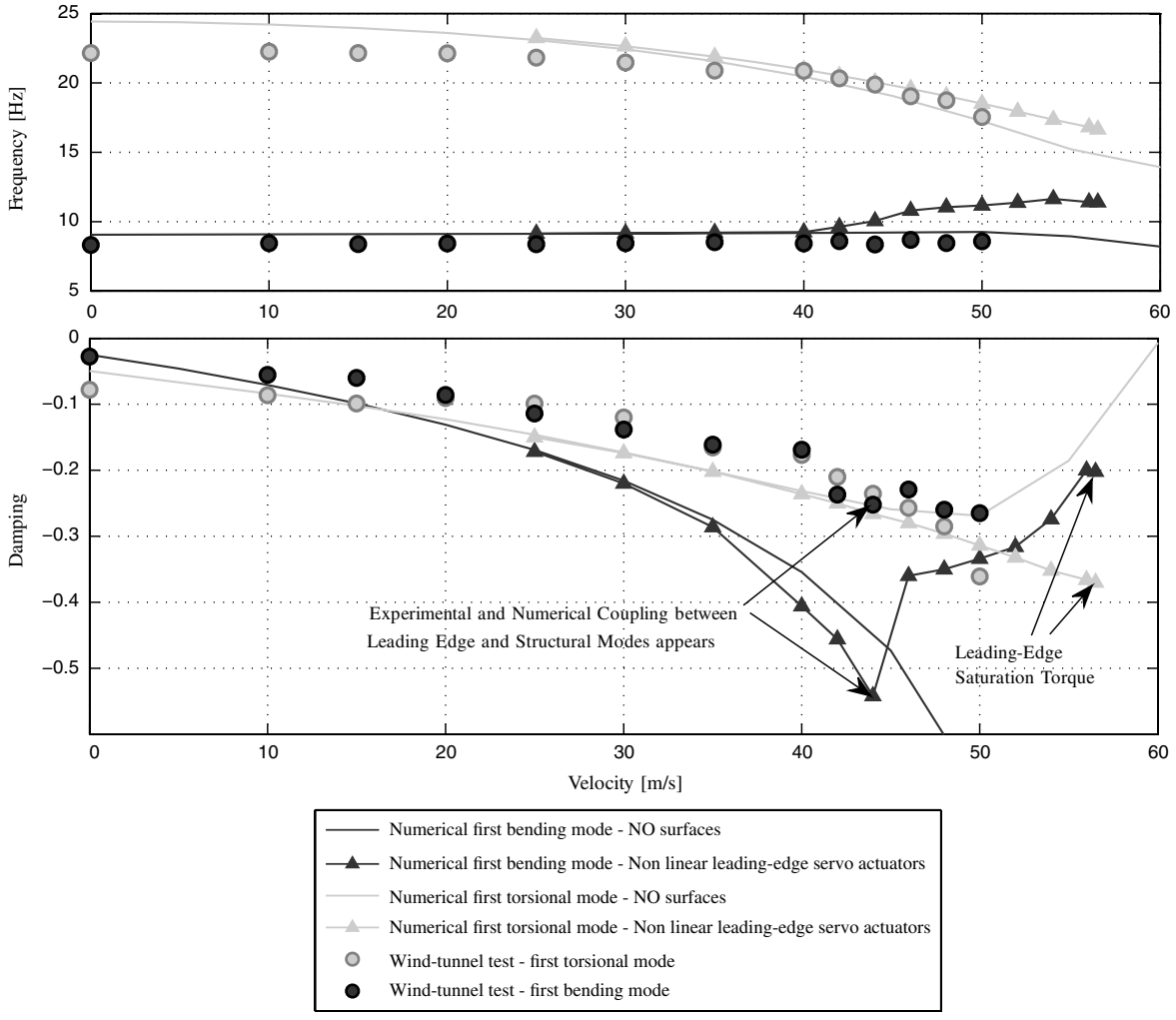

Fig. 17 Numerical vs experimental *V–g* plot.

each frequency peak is repeated 4 times. The frequency response functions were measured on four accelerometers located on the wing and the procedure was repeated in the speed range from 10 to 50 m/s with speed increments of 5 and 2.5 m/s, in the speed ranges of 10–40 and 40–50 m/s, respectively. Once the experimental data collection was completed, identification was carried out using the autoregressive exogenous (ARX) algorithm [33] implemented in MATLAB. The results obtained (black circles and gray squares) in Fig. 17 are noted in a V–g plot together with the numerical ones, computed with ASE numerical models. In particular, both numerical results obtained considering the control surfaces as fixed (black and gray lines) or including the servoactuators dynamics (black and gray triangles), are reported. Looking at the final V–g plot reported in Fig. 17, it appears to be a good correlation between numerical and experimental frequency and damping estimations for different wind-tunnel speeds. It is interesting to highlight, on numerical results, the effect of servoactuators on wing flutter behavior. While considering control surfaces as fixed, the wing shows a classical bending-torsion flutter around 60 m/s, perfectly matching the preliminary results obtained on the full scale target aircraft. Introducing servoactuators dynamics into the numerical model heavily changes wing flutter behavior. In fact, up to a speed of 43 m/s, the PID control implemented on four control surfaces increases the aeroelastic damping of the bending mode, with a very low influence on the torsional one. For speeds higher than this, a strong coupling between servoactuators dynamics and structural modes appears. In particular, damping associated with the bending mode decreases while the torsion one increases. The reason is that lift variation due to torsion mode results in a servoactuator reaction aiming at reducing the lift itself; on the other hand, any change of kinematic angle of attack related to the bending mode is amplified by PID implemented into servoactuators. Finally, flutter appears around 56 m/s when maximum allowable torque values are reached. From the experimental point of view, a complete matching of numerical results was not possible, mainly because, for safety reasons, the testing speed was limited to 50 m/s. Nevertheless, some kind of numerical–experimental correlation can be pointed out. Looking at Fig. 17, up to 48 m/s, the interaction among servoactuators dynamics and structural modes appears to introduce very little modification in the modal participating mechanism between bending and torsion. However, in the same figure, it is possible to appreciate the decrease of torsional mode frequency, as it appears from the numerical results. Finally, observing Fig. 18, where frequency response functions measured on the wing, representing the ratio between TEO acceleration and TEO aileron rotation, are reported, it is possible to see an increasing coupling mechanism between first bending and torsion modes, which could be considered as a symptom of approaching flutter.

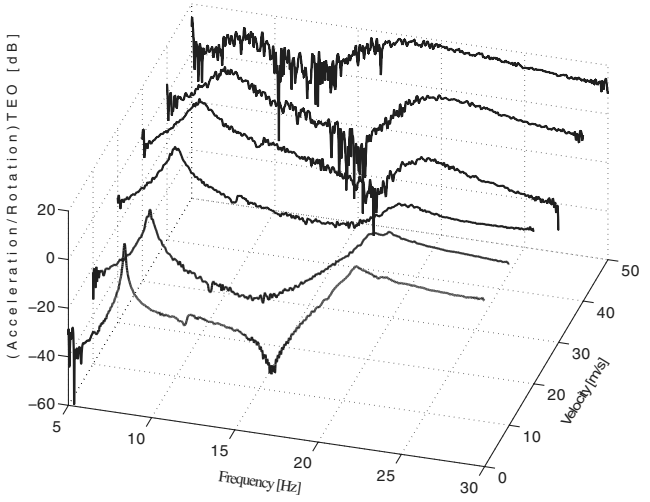

Fig. 18 Experimental frequency response function evaluation: dependency upon velocity.

C. Modal Control

The final wind-tunnel stage was devoted to modal control investigations. The experimental setup was the same as was already adopted during previous testing campaigns. In particular, for an assigned wind-tunnel speed, equal to 30 m/s, the wing was self-excited by a sine-dwell excitation, produced by oscillating the TEO surface in the frequency range from 5 to 27 Hz. Even if a complete wind-tunnel campaign for different speeds is necessary to completely characterize the ILAF-based control system, the preliminary results appear very encouraging [34]. Figures 19 and 20 show the frequency response functions, as a ratio between output from the TEO accelerometer over TEO rotation, as experimentally measured and identified using the same ARX algorithm adopted during flutter identification. It is possible to see that a peak reduction of nearly 10 and 12 dB was measured for bending and torsion modes, respectively. This damping level is obtained when all four control surfaces are controlled together. Additional results are shown with two more diagrams: Figs. 21 and 22 show both actually measured and required control surface rotations. When experimental identification of each control surface (without aerodynamic load effects) had been run (please refer to Figs. 8 and 9), phase was measured. Operating with aerodynamic loads again allows phase measurement of the four systems: this was performed directly from Figs. 21 and 22. Table 6 provides values measured in both conditions: it is possible to see that only when working with the LEO control surface, is the phase significantly affected, while all other surfaces are almost unaffected by aerodynamic loads. Figure 23 shows torque measured during the modal control session: it is possible to see that the constraints on maximum torque for both leading- (0.4 N/m) and trailing-edge (0.1 N/m) control surfaces are satisfied. To check the robustness of adopted control architecture and to understand properly the contribution of each of the four control surfaces on wing

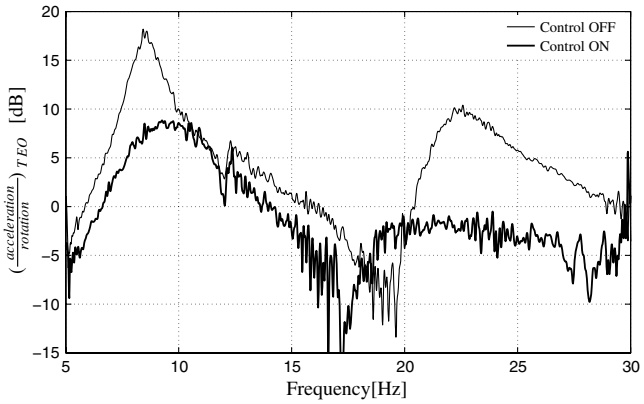

Fig. 19 Measured frequency response functions (tip acceleration over TEO excitation) with and without control.

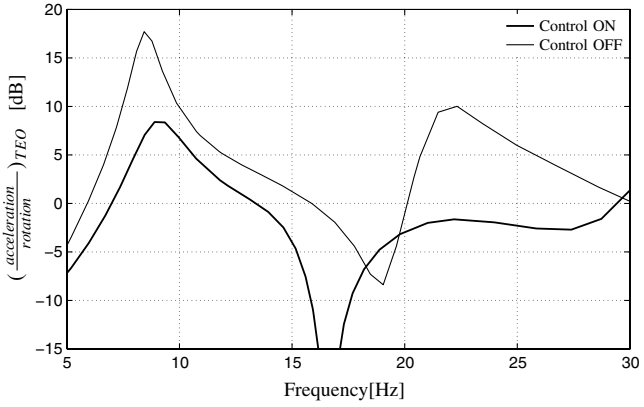

Fig. 20 Identified frequency response functions (tip acceleration over TEO excitation) with and without control.

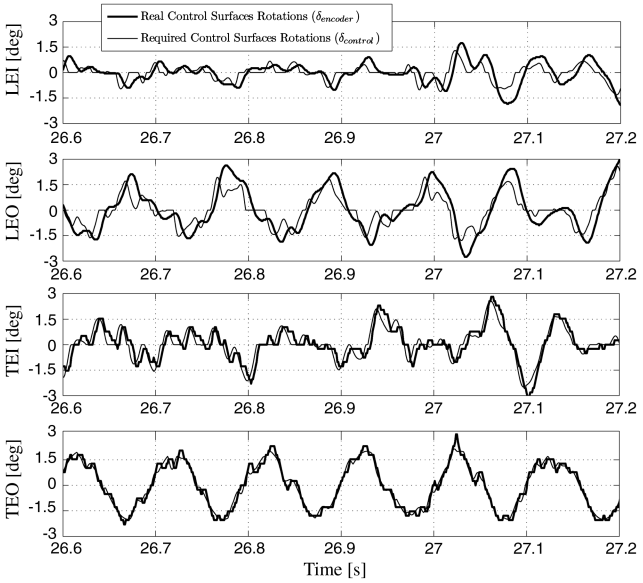

Fig. 21 Control rotations applied during modal control (bending mode).

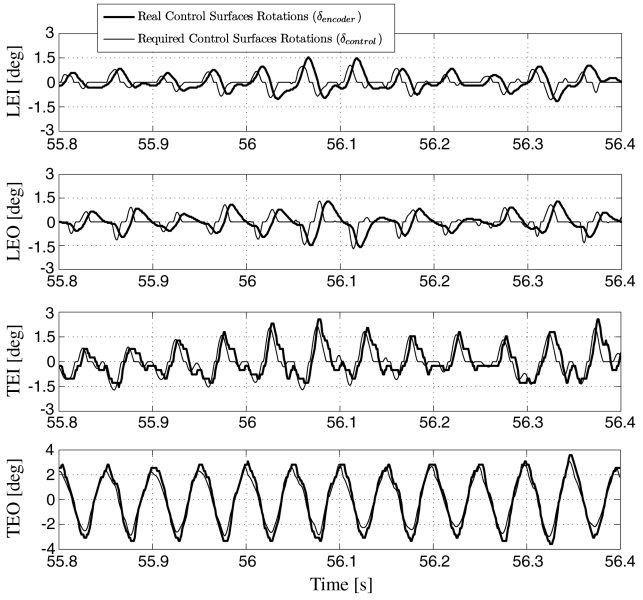

Fig. 22 Control rotations applied during modal control (torsion mode).

behavior, a more detailed test was run, where control system was sectioned, in order to have only some control surfaces working. Even in this case the measured and the identified transfer functions are reported. From Fig. 24, it appears that when the wing inboard strip is deactivated, peak acceleration values augment slightly. This may lead to the conclusion that damping is mostly controlled by outer strip control surfaces. It also appears that inboard strip control surfaces do diminish any possible coupling between bending and torsion modes. By deactivating only bending control on the inner strip, it appears that torsion control increases in capability, but

Table 6 Phase experimental identification

	Without Aeroloads	With Aeroloads
LEI	50 deg	52 deg
LEO	45 deg	55 deg
TEI	10 deg	15 deg
TEO	8 deg	15 deg

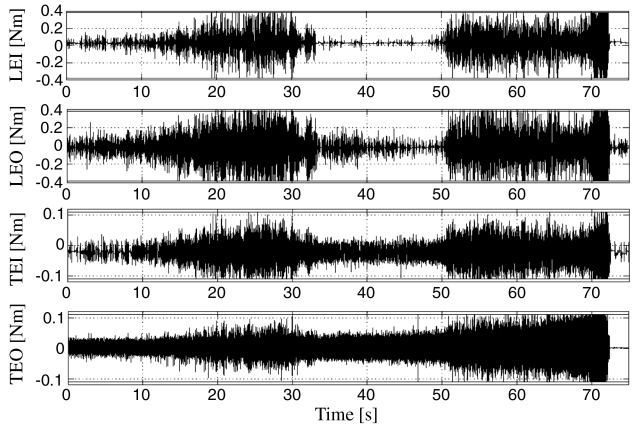

Fig. 23 Control torques applied during modal control.

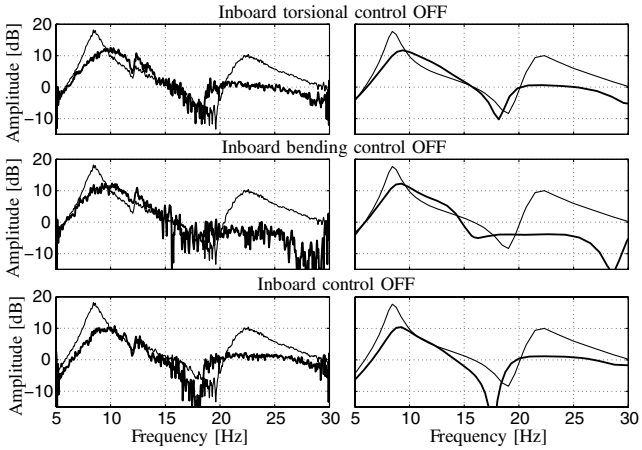

Fig. 24 Effect of different control surfaces on measured frequency response functions.

possible coupling may rise at a lower frequency; hence this solution looks rather misleading. Vice versa, by deactivating only torsion control over the inner strip leads to useless results. Four surfaces acting together appear to be the optimal choice in controlling wing modes.

VI. Conclusions

This paper presented the numerical and experimental activities related to the design and manufacturing of a wind-tunnel wing model, equipped with four control surfaces, to be installed in the X-DIA aeroelastic demonstrator. The design of the wing model is based on a constant Froude scaling with respect to a reference full-scale target aircraft. Each control surface is driven by an electric motor embedded into the central part of the wing. The aeroservoelastic model was tuned on the basis of wind-tunnel results, where both frequency response functions and wing loads were measured by means of accelerometers embedded into the model and by using an aerodynamic balance used to clamp the root of the wing main spar. The experimentally correlated aeroservoelastic model was used to predict the flutter behavior of the wing and to design the control system for modal control purpose.

A generalization of the original ILAF control architecture was developed and implemented, where control forces are not proportional to local velocity but to modal velocity. In particular, two mode shapes of the wing model were initially controlled, first bending and torsion modes. The ILAF control methodology demonstrated a good capability of shaping wing modes already at 30 m/s (and up to 42 m/s, which, by chance, is the maximum speed tested), with good performances related both to bending and torsion. Indeed, a reduction of 10 and 12 dB on the acceleration peak related

to first bending and torsion modes, respectively, was experimentally verified. The adopted control architecture appears as noticeably robust: even by switching off the single control surfaces the capability to damp first bending and torsion modes remains remarkable, even if the best performance is obtained by using all four control surfaces. Finally, from the user point of view, the experimental activity demonstrated that ILAF control architecture can be easily tuned, using a limited number of control gains having a clear physical meaning.

Future developments will include at first a complete characterization of the modal control here proposed for the whole range of wind-tunnel speeds, then an extension of the aeroservoelastic model so to take into account in a more precise way the presence of free play, especially connected with actuators gear heads, and their effects on control performances. Finally, the modal control system here presented will be coupled to a roll maneuver enhancement control system, now under development, so to be able to optimize the aircraft roll performances in terms of both static and dynamic structural requirements, taking advantage of the presence of redundant control surfaces.

Acknowledgments

The numerical and experimental activities related to the X-DIA active wing concept have been partially funded by the European Union under the Fifth Research Framework, through the project Active Aeroelastic Aircraft Structures (3AS), Project No. GRD-1-2001-40122. The authors would like to thank Gabriele Campanardi and Donato Grassi for their generous help during the wind-tunnel test session, Alessandro Toso for providing the implementation of the ARX algorithm, and Mauro Terraneo for his generous help during FEM model updating.

References

[1] Thornton, S. V., "Reduction of Structural Loads Using Maneuver Load Control on the Advanced Fighter Technology Integration (AFTI) Mission Adaptive Wing," NASA TM-4526, Sept. 1993.

[2] Stanewsky, E., "Adaptive Wing and Flow Control Technology," *Progress in Aerospace Sciences*, Vol. 37, No. 7, 2001, pp. 583–667. doi:10.1016/S0376-0421(01)00017-3

[3] Eller, D., and Heinze, S., "An Approach to Induced Drag Reduction and its Experimental Evaluation," *Proceedings of the 45th AIAA/ASME/ASCE/AHS/ASC Structures, Structural Dynamics and Materials Conference*, AIAA, Reston, VA, 19–22 April 2004.

[4] Pendleton, E., Bessette, D., Field, P., Miller, G., and Griffin, K., "Active Aeroelastic Wing Flight Research Program: Technical Program and Model Analytical Development," *Journal of Aircraft*, Vol. 37, No. 4, 2000, pp. 554–561. doi:10.2514/2.2654

[5] Perry, B., and Cole, S. R., "Summary of an Active Flexible Wing Program," *Journal of Aircraft*, Vol. 32, No. 1, 1995, pp. 10–15. doi:10.2514/3.46677

[6] Woods-Vedler, J. A., Pototzky, A., and Hoadley, S., "Rolling Maneuver Load Alleviation Using ACtive Control," *Journal of Aircraft*, Vol. 32, No. 1, 1995, pp. 68–76. doi:10.2514/3.46685

[7] Lucia, D. J., "The SensorCraft Configurations: A Non-Linear AeroServoElastic Challenge for Aviation," *Proceedings of the 46th AIAA/ASME/ASCE/AHS/ASC Structures, Structural Dynamics and Materials Conference*, AIAA, Reston, VA, 18–21 April 2005.

[8] Silva, W. A., Vartio, E., Shimko, A., Kvaternik, R. G., Eure, K. W., and Scott, R., "Development of Aeroservoelastic Analytical Models and Gust Load Alleviation Control Laws of a SensorCraft Wind-Tunnel Model Using Measured Data," *Proceedings of the IFASD International Forum on Aeroelasticity*, International Forum on Aeroelasticity and Structural Dynamics, Stockholm, Sweden, 17–20 June 2007.

[9] Liebeck, R. H., "Design of the Blended Wing Body Subsonic Transport," *Journal of Aircraft*, Vol. 41, No. 1, 2004, pp. 10–25. doi:10.2514/1.9084

[10] Abel, I., "Evaluation of a Technique for Determining Airplane Aileron Effectiveness and Roll Rate by Using an Aeroelastically Scaled Model," NASA TN D-5538, Nov. 1969.

[11] Nissim, E., and Abel, I., "Development and Application of an Optimization Procedure for Flutter Suppression Using the Aerodynamic Energy Concept," NASA TP-1137, Feb. 1978.

[12] Lock, W., Kordes, E., McKay, J., and Wykes, J., "Flight Investigation of a Structural Mode Control System for XB-70 Aircraft," NASA TN D-7420, May 1973.

[13] Malecek, J., Cecrdle, J., Scotti, A., Ricci, S., Kiessling, F., and Klimmek, T., "Dynamic Response Analysis and Experimental Validation of the X-DIA Demonstrator Component Model," *Proceedings of the IFASD International Forum on Aeroelasticity*, International Forum on Aeroelasticity and Structural Dynamics, Munich, Germany, 28 June –1 July 2005.

[14] Ricci, S., Scotti, A., Malecek, J., and Cecrdle, J., "Experimental Investigations of a Vibration Suppression System for a Three Surface Aeroelastic Model," *Proceedings of the 46th AIAA/ASME/ASCE/AHS/ASC Structures, Structural Dynamics and Materials Conference*, AIAA, Reston, VA, 18–21 April 2005.

[15] Schweiger, H., and Suleman, A., "The European Research Project Active Aeroelastic Aircraft Structures," *Proceedings of the IFASD International Forum on Aeroelasticity*, International Forum on Aeroelasticity and Structural Dynamics, Amsterdam, The Netherlands, 4–6 June 2003.

[16] Roskam, J., *Airplane Design*, Roskam Aviation and Engineering Corp., Ottawa, KS, 1985.

[17] Rae, W., and Pope, A., *Low Speed Wind Tunnel Testing*, Wiley, New York, 1984.

[18] Ricci, S., and Scotti, A., "Aeroelastic Testing of a Three Surface Aircraft," *Proceedings of the 47th AIAA/ASME/ASCE/AHS/ASC AIAA/ASME/ASCE/AHS/ASC Structures, Structural Dynamics and Materials Conference*, AIAA, Reston, VA, 1–4 May 2006.

[19] Scotti, A., Ricci, S., and Quaranta, G., "Active Control of a Three Surface Wind Tunnel Aeroelastic Demonstrator: Modelling and Correlations," *Proceedings of the IFASD International Forum on Aeroelasticity*, International Forum on Aeroelasticity and Structural Dynamics, Munich, Germany, June 28–July 1 2005.

[20] Vepa, R., "On the Use of Pade Approximants to Represent Unsteady Aerodynamic Loads for Arbitrarily Small Motions of Wings," *Proceedings of the 14th American Institute of Aeronautics and Astronautics, Aerospace Sciences Meeting*, AIAA, Washington, D.C., 1976.

[21] Roger, K., "Airplane Math Modeling Methods for Active Control Design," AGARD CP-228, April 1977.

[22] Karpel, M., "Design for Active Flutter Suppression and Gust Alleviation Using State-Space Aeroelastic Modeling," *Journal of Aircraft*, Vol. 19, No. 3, 1982, pp. 221–227. doi:10.2514/3.57379

[23] Karpel, M., "Reduced Order Aeroelastic Models via Dynamic Residualization," *Journal of Aircraft*, Vol. 27, No. 5, 1990, pp. 449–455. doi:10.2514/3.25297

[24] Karpel, M., "Physically Weighted Approximation of Unsteady Aerodynamic Forces Using the Minimum-State Method," NASA TP-3025, March 1991.

[25] Morino, L., Mastroddi, F., De Troia, F., Ghiringhelli, G. L., and Mantegazza, P., "Matrix Fraction Approach for Finite-State Aerodynamic Modeling," *AIAA Journal*, Vol. 33, No. 4, 1995, pp. 703–711. doi:10.2514/3.12381

[26] Antoulas, A., and Sorensen, D., "Approximation of Large-Scale Dynamical Systems: An Overview," *International Journal of Applied Mathematics and Computer Science*, Vol. 11, No. 5, 2001, pp. 1093–1121.

[27] Pasinetti, G., and Mantegazza, P., "Single Finite States Modeling of Aerodynamic Forces Related to Structural Motions and Gusts," *AIAA Journal*, Vol. 37, No. 5, May 1999, pp. 604–612. doi:10.2514/2.760

[28] Mantegazza, P., and Quaranta, G., "A Robust Technique to Create Reduced Order Models for Aircraft Aerodynamic Unsteady Loads" (to be published).

[29] Ricci, S., Scotti, A., Cecrdle, J., and Malecek, J., "Active Control of Three-Surface Aeroelastic Model," *Journal of Aircraft*, Vol. 45, No. 3, 2008, pp. 1002–1013. doi:10.2514/1.33303

[30] Ricci, S., Scotti, A., and Zanotti, D., "Control of an All-Movable Foreplane for a Three Surfaces Aircraft Wind Tunnel Model," *Journal of Mechanical Systems and Signal Processing*, Vol. 20, No. 5, 2006, pp. 1044–1066.

[31] Dozio, L., and Mantegazza, P., "Real Time Distributed Control Systems Using RTAI," *Proceedings of International Symposium on Object-Oriented Real-Time Distributed Computing*, ISORC, Hakodate, Japan, 14–16 May 2003, pp. 11–18.

[32] Ghiringhelli, G., Lanz, M., and Mantegazza, P., "Active Flutter Suppression for a Wing Model," *Journal of Aircraft*, Vol. 27, No. 4, 1990, pp. 334–341.
doi:10.2514/3.25277

[33] Qin, S. J., and Badgwell, T. A., "A Survey of Industrial Model Predictive Control Technology," *Control Engineering Practice*, Vol. 11, No. 7, 2003, pp. 733–764.
doi:10.1016/S0967-0661(02)00186-7

[34] De Gaspari, A., and Riccobene, L., "Progetto e Validazione di un Modello di Ala a Freccia Negativa con Controllo Attivo Multi-Superficie," M.S. Thesis, Politecnico di Milano, 2006 (in Italian).

C. Cesnik
Associate Editor